Energy Reports 14 (2025) 566–578

Contents lists available at ScienceDirect

Energy Reports

journal homepage: www.elsevier.com/locate/egyr

Research paper

AC voltage and reactive power control in DFIG-based wind farms: A comparative study for mitigating sub-synchronous resonance in compensated and weak networks

Jorge Vega-Herrera [a], Stevens Fuentes-Flores [a], Diego Ortiz-Villalba [b,*], Jacqueline Llanos [b], Alex Villamarín-Jácome [b,c], Marcelo Cortes-Carmona [a], Danny Espín-Sarzosa [d]

[a] Department of Electrical Engineering, University of Antofagasta, Avda. Angamos 601, Antofagasta 1270300, Chile
[b] Department of Electrical Electronic and Telecommunication, Universidad de las Fuerzas Armadas ESPE, Sangolqui 171103, Ecuador
[c] Department of Electrical Engineering, University of Chile, Avda. Beauchef 851, 8370456, Chile
[d] Department of Electrical Engineering, Universidad Técnica Federico Santa María, Valparaiso 2390123, Chile

ARTICLE INFO

Keywords:
AC voltage control
Doubly fed induction generator
Grid side converter
Reactive power control
Small-signal stability analysis
Stability regions

ABSTRACT

Integrating Doubly-Fed Induction Generator (DFIG)-based wind farms into weak and series-compensated systems may introduce significant subsynchronous resonance (SSR) risks, compromising system stability. This paper presents a detailed comparative analysis of two control strategies, reactive power control, and AC voltage control, implemented in the outer control loops related to the grid side converter (GSC) to mitigate SSR in DFIG-based systems. The comparisons are based on modal analysis, and the dynamic risk of SSR is investigated by evaluating several operating conditions and key control parameters. This includes different levels of series compensation, weakness, phase-locked loop (PLL) bandwidth, and current control parameters associated with the rotor-side converter (RSC). The results demonstrate that AC voltage control provides superior dynamic performance and less SSR risk damping, especially in highly compensated grids where reactive power control is unstable. Furthermore, sensitivity analysis highlights the critical role of RSC tuning and PLL bandwidth in maintaining system stability to avoid SSR risks. These findings offer practical insights for control design strategies in DFIG-based wind farms, particularly for applications in weak and compensated grids, enhancing grid reliability and reducing the risk of SSR.

1. Introduction

In recent years, the integration of wind energy generation has expanded rapidly worldwide, becoming crucial for sustainable energy development. By 2023, the global cumulative wind power capacity surpassed 1 TW, with 117 GW of new installations. This represents a 13 % annual growth rate (GWEC, 2024). Among various technologies in wind energy conversion systems (WECS), which operate at variable speeds, the doubly-fed induction generator (DFIG) is the most commonly employed in large-scale wind farms (Okedu, 2022; Din et al., 2022; Soomro et al., 2023). WECS, based on DFIG, operates at variable speed and is cost-effective regarding power electronics. The converter is connected to the DFIG rotor, so its power capacity is only part of the total generator capacity, ranging from 25 % to 30 % approximately (Hussain et al., 2024; Loncarski et al., 2023). Furthermore, DFIG allows for independent control of active and reactive power, enabling the integration and operation of the grid under variable wind conditions (Hussain et al., 2024; Fan and Miao, 2021; Abdeen et al., 2020).

However, the growing integration of WECS based on DFIG introduces significant challenges in terms of power system stability. These challenges are particularly complicated when generators are connected at weak buses and/or through series-compensated transmission lines (Din et al., 2022; Task Force on Wind SSO, 2020; Cheng et al., 2023). In these conditions, stability issues due to subsynchronous resonance (SSR) become a concern (Din et al., 2022; Task Force on Wind SSO, 2020; Cheng et al., 2023). SSR issues have been observed in power systems as undamped oscillations of relevant electrical variables. The oscillation frequency is typically below the system frequency, and it may cause damage to both the wind turbine and the transmission system equipment (Irwin et al., 2011). Several real-world SSR have been reported in

* Corresponding author.
E-mail address: ddortiz5@espe.edu.ec (D. Ortiz-Villalba).

https://doi.org/10.1016/j.egyr.2025.06.005
Received 9 January 2025; Received in revised form 12 May 2025; Accepted 14 June 2025
Available online 24 June 2025
2352-4847/© 2025 The Authors. Published by Elsevier Ltd. This is an open access article under the CC BY license (http://creativecommons.org/licenses/by/4.0/).

various power systems. In 2007 Minnesota, oscillations with frequencies of 9.44 Hz were observed as poorly damped (Task Force on Wind SSO, 2020; Cheng et al., 2022; Fan et al., 2022). Similar phenomena were noticed in Texas in 2009 (Task Force on Wind SSO, 2020; Irwin et al., 2011); China in the years 2012–2013 (Task Force on Wind SSO, 2020; Xie et al., 2017); Texas 2017 (Task Force on Wind SSO, 2020). The oscillation frequencies of these events were 20–30 Hz, 6–9 Hz, and 22–26 Hz, respectively (Fan and Miao, 2021). Some consequences of these oscillatory phenomena are overcurrent, power plant overvoltages, and damage to DFIG circuits (Cheng et al., 2023; Wang et al., 2015). In general, these SSR occur when generators are connected to the grid by compensated transmission lines or where the point of common coupling (PCC) has a low short-circuit level (Din et al., 2022; Cheng et al., 2023; Liu et al., 2018). These problems are described in the literature as (SSR) (Xie et al., 2017), subsynchronous frequency control interaction (SSCI) (Irwin et al., 2011), or subsynchronous interaction (SSI) (Gu et al., 2019). This work adopts the term SSR to refer to these problems.

In the literature, it has been shown that the implemented control system also has significant impacts. The actual DFIG operates in grid-following mode, where the control system is typically implemented in a synchronous reference frame dq. A phase-locked loop (PLL) is generally used to synchronize the generator with the grid for this operation mode. Several studies on SSR have reported that PLL has a significant impact (Fan and Miao, 2021; Liu et al., 2018; Yan et al., 2020). In (Liu et al., 2018), it is shown that the low bandwidth of the PLL allows for a better dynamic response under weak grids, and the high bandwidth may exacerbate SSR problems. In addition to the PLL, other control systems also impact on the SSR, such as the control parameters of the rotor side converter (RSC) and the grid side converter (GSC) of the DFIG (Wang et al., 2015). Reference (Wang et al., 2015) states that both RSC and GSC impact SSR, particularly RSC (Irwin et al., 2011; Virulkar and Gotmare, 2016; Xu and Zhao, 2019). The influence of the RSC on the SSR is essential for the interaction between the generator and the compensation level of the transmission system (Virulkar and Gotmare, 2016).

Given the above challenges, various strategies to mitigate SSR have been proposed. In (Xu and Zhao, 2019), an analytical model of a DFIG is proposed to study SSR in DFIGs, highlighting the importance of properly tuning the control parameters. This means that a proper tuning process may prevent compensating SSR due to transmission lines. Similarly, (Yan et al., 2020) proposes a method based on an active disturbance rejection control and demonstrates its effectiveness in reducing SSR risks in series-compensated grids. Other works have highlighted the influence of grid strength on SSR. In (Virulkar and Gotmare, 2016), adaptive control strategies for DFIG connected to weak grids are proposed. Furthermore, (Gu et al., 2019) reviewed the SSR in DFIG, highlighting the need for control systems that can adapt to both the strength of the grid and the presence of series compensation. These studies highlight the complexity of maintaining stability in wind farms, especially as the penetration of DFIG increases. It is worth noting that while converter controls have been used for mitigation, a direct, detailed comparison of the inherent SSR mitigation capability is provided by simply choosing between the two standard GSC outer control objectives, such as AC voltage or reactive power control and evaluating their performance across both series-compensated and weak operating conditions using modal analysis is a specific, unexplored comparison and needed.

Most studies focus on the impacts of inner control loops, i.e., current controllers related to RSC or GSC and the PLL. In contrast, the effects of outer controllers, such as reactive power or voltage control, still need to be fully understood. This leads to a gap in understanding the implications of control strategies on SSR when the DFIG is connected to weak systems, with or without series compensated transmission networks. This work bridges this gap by systematically comparing two outer control loops for the GSC, reactive power, and voltage control. The impacts of the outer control on SSR are investigated using modal analysis. This work conducts a comprehensive investigation, subjecting relevant control system parameters, such as PLL and current RSC control, to sensitivity analysis. It also explores different operation conditions, including weak systems, active power injection, and compensation levels. The results are then rigorously validated by dynamic simulations.

This work presents three main contributions to integrating DFIG-based wind farms into weak and series-compensated power systems facing SSR risks. First, it provides a detailed comparative analysis of reactive power control and voltage control strategies implemented in the outer control loops of the GSC in the DFIG, focusing on their effectiveness in mitigating SSR. This topic remains insufficiently explored in the context of weak and compensated grids. Second, it introduces a modeling framework specifically designed to assess the impact of these outer control strategies on SSR behavior, enabling systematic and consistent evaluation across different operating conditions. While EMT-based models have been widely used for SSR studies, this contribution emphasizes the importance of control-oriented modeling in understanding the influence of high-level control structures. For this purpose, modal analysis is used. Third, the study rigorously validates the comparative performance of the control strategies using modal analysis and dynamic simulations, demonstrating that voltage control provides superior SSR mitigation under weak grid and high series-compensation conditions. These findings offer practical insights for improving the control design of DFIG-based wind farms to enhance stability and avoid SSR risks.

The remainder of this article is organized as follows. 2 presents the test system model. 3 presents the case studies, results, and discussions. Finally, 4 summarizes the main conclusions and related future work.

2. Test system model

This section details the mathematical model of the system used in this work, depicted in Fig. 1. The test system consists of a DFIG connected to the grid through two transmission lines, one of which includes series compensation. The stator of the DFIG is directly connected to the PCC, while the rotor is interfaced with the grid through voltage source converters (VSCs) configured in a back-to-back arrangement. This configuration includes two converters with distinct control strategies: the RSC and the GSC. The GSC is connected to the PCC through an LC filter.

The system is modeled using dq reference frame, which is standard for such analyses. The transient effects associated with switching of power electronic devices are neglected, as their dynamics are significantly faster than those involved in the SSR and SSCI studies (Fan and Miao, 2021; Kunjumuhammed et al., 2019). This simplification is widely used in the literature because it allows the use of linearized models for modal analysis (Irwin et al., 2011; Wang et al., 2015; Kunjumuhammed et al., 2019; Fan et al., 2011). These assumptions ensure both the accuracy and relevance of the model for the intended study.

Each model component is described below, including the turbine generator mechanical drive train model, the DFIG, DC link, LC filter, inner current, and outer controllers. The model is developed using per-unit values, with the system parameters in Table 3 of the Appendix.

2.1. Turbine generator mechanical drive train model

The driven train is represented by a two-mass, as described in (Kunjumuhammed et al., 2019). The equations governing the dynamics of this model are given by:

$$2H_g\frac{d\omega_r^{pu}}{dt} = T_g - T_e + D_{tg}\left(\omega_t^{pu} - \omega_r^{pu}\right) - D_g\omega_r^{pu} \tag{1}$$

$$2H_t\frac{d\omega_t^{pu}}{dt} = T_m - T_g + D_{tg}\left(\omega_r^{pu} - \omega_t^{pu}\right) - D_t\omega_t^{pu} \tag{2}$$

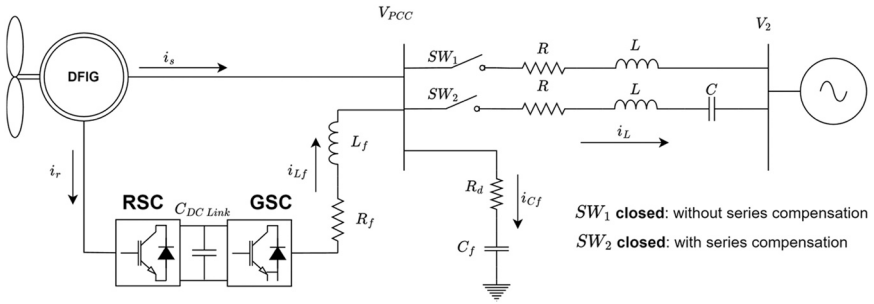


Fig. 1. Test system.

$$\frac{dT_g}{dt} = k_{tg}\left(\omega_t^{pu} - \omega_r^{pu}\right) \tag{3}$$

where ω_r^{pu} and ω_t^{pu} denote the speeds of the rotor and turbine (in per unit), respectively. T_m, T_e, T_g represent the mechanical, electromagnetic torques and the torque between the two masses, respectively (in per unit). The parameters H_g and H_t are the inertia constants of the generator and turbine, respectively (in seconds), while D_{tg}, D_t and D_g are the damping coefficients for the drive train, turbine, and generator (in per unit). The stiffness of the drive system is denoted by k_{tg} (in per unit). For a more detailed description and derivation, readers are referred to (Fan et al., 2011).

2.2. Doubly-fed induction generator

The electrical dynamics of the DFIG are derived from Kirchhoff's Voltage Law (KVL) applied to the equivalent circuit in the dq reference frame (see Fig. 2). The differential equations governing the stator and rotor voltages are expressed as:

$$v_{sDQ} = -R_s i_{sDQ} + \frac{1}{\omega_b}\frac{d\psi_{sDQ}}{dt} + j\omega_e^{pu}\psi_{sDQ} \tag{4}$$

$$v_{rDQ} = -R_r i_{rDQ} + \frac{1}{\omega_b}\frac{d\psi_{rDQ}}{dt} + j\omega_{SL}^{pu}\psi_{rDQ} \tag{5}$$

$$\omega_{SL}^{pu} = \omega_e^{pu} - \omega_r^{pu} \tag{6}$$

where v_{sDQ} and v_{rDQ} represent the stator and rotor voltages (in per unit), respectively. The subscripts D and Q indicate the components of voltages and currents along the d-axis and q-axis, respectively. R_s and R_r denote the stator and rotor resistances (in per unit), while i_{sDQ} and i_{rDQ} represent the stator and rotor currents (in per unit). The base electrical speed is given by ω_b (in rad/s). ω_e^{pu} and ω_{SL}^{pu} represent the angular electrical velocity and the angular slip (in per unit), respectively. ψ_{sDQ} and ψ_{rDQ} represent the magnetic fluxes in the stator and rotor (in per unit), respectively. Further details of the DFIG equations can be found in (Krause et al., 2013).

The active and reactive power at the terminals of the stator and rotor in the induction machines can be expressed as

$$P_s = v_{sD} i_{sD} + v_{sQ} i_{sQ} \tag{7}$$

$$Q_s = v_{sQ} i_{sD} - v_{sD} i_{sQ} \tag{8}$$

$$P_r = v_{rD} i_{rD} + v_{rQ} i_{rQ} \tag{9}$$

$$Q_r = v_{rQ} i_{rD} - v_{rD} i_{rQ} \tag{10}$$

$$T_e = \psi_{rQ} i_{rD} - \psi_{rD} i_{rQ} \tag{11}$$

where P_s and Q_s represent the active and reactive powers at the stator, respectively, while P_r and Q_r represent the active and reactive powers at the rotor (all in per unit).

2.3. DC ink dynamics

The DC link model is derived by applying Kirchhoff's Current Law (KCL) to the circuit, depicted in Fig. 3. The equations are based on a power flow balance between the RSC, GSC, and the capacitor, neglecting

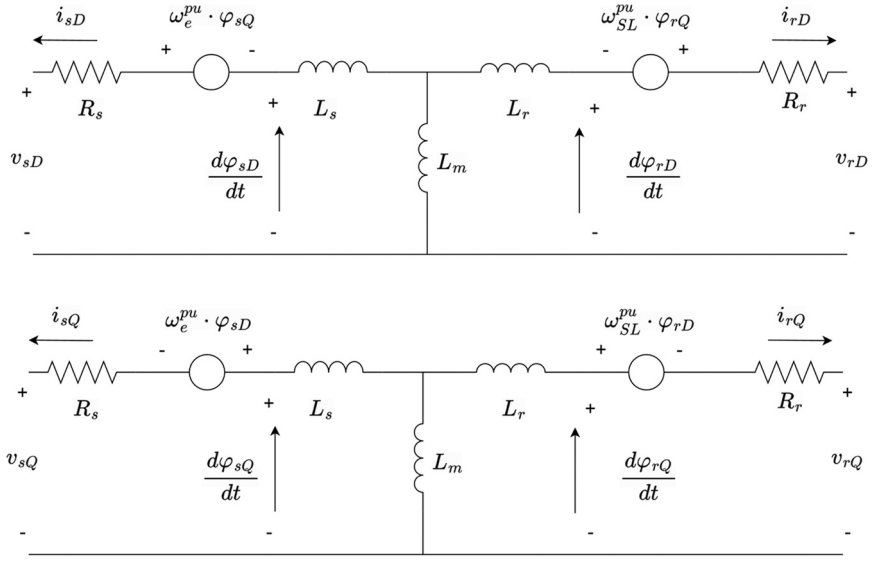


Fig. 2. Equivalent circuit for the voltage equations of the DFIG.

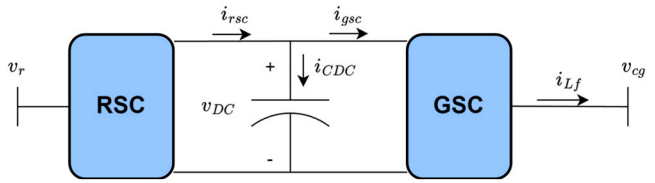


Fig. 3. Power flow balance in DC link.

converter losses (Fan and Miao, 2021; Kunjumuhammed et al., 2019). The dynamics of the DC link can be expressed as:

$$\frac{C_{\mathrm{DC}}}{2\omega_{\mathrm{b}}}\frac{\mathrm{d}v_{\mathrm{DC}}^2}{\mathrm{d}t} = P_{\mathrm{rsc}} - P_{\mathrm{gsc}} \tag{12}$$

where C_{DC} represents the DC link capacitance, v_{DC} denotes the DC link voltage, P_{rsc} is the power flow through the RSC, and P_{gsc} is the power flow through the GSC (all in per unit).

2.4. LC filter

The GSC is connected to the grid through an LC filter, modeled by applying KVL to the filter circuit (see Fig. 1):

$$\frac{L_{\mathrm{f}}}{\omega_{\mathrm{b}}}\frac{\mathrm{d}i_{\mathrm{LfDQ}}}{\mathrm{d}t} = v_{\mathrm{cgDQ}} - v_{\mathrm{sDQ}} - R_{\mathrm{f}}i_{\mathrm{LfDQ}} + j\omega_{\mathrm{e}}^{\mathrm{pu}}i_{\mathrm{LfDQ}}L_{\mathrm{f}} \tag{13}$$

$$\frac{C_{\mathrm{f}}R_{\mathrm{d}}}{\omega_{\mathrm{b}}}\frac{\mathrm{d}v_{\mathrm{CfDQ}}}{\mathrm{d}t} = v_{\mathrm{sDQ}} - v_{\mathrm{CfDQ}} + jC_{\mathrm{f}}R_{\mathrm{d}}v_{\mathrm{CfDQ}}\omega_{\mathrm{e}}^{\mathrm{pu}} \tag{14}$$

where L_{f} represents the inductance of the LC filter, i_{LfDQ} is the current through the LC filter, v_{cgDQ} is the voltage at the output of the GSC, and v_{sDQ} is the voltage at the stator terminals (all in per unit). The resistance of the LC filter is denoted by R_{f}, C_{f} is the capacitance of the LC filter, and R_{d} is the damping resistance. The voltage across the LC filter capacitor is denoted by v_{CfDQ} (all in per unit). For a discussion of LC filter design and its role in DFIG systems, see (Kunjumuhammed et al., 2019).

2.5. Transmission network model

In this work, the DFIG generator is connected to the grid through a transmission line. This may or may not have series compensation, which is determined by the switches, SW1 and SW2. As shown in Fig. 1, with SW1 closed and SW2 open, the control panel is connected through a transmission system without series compensation. With SW2 closed and SW1 open, the control panel is connected via a transmission line with series compensation. The model for the case without series compensation is obtained from the application of KVL between V_{PCC} and V_2. Thus, the model is given by:

$$\frac{L}{\omega_{\mathrm{b}}}\frac{\mathrm{d}i_{\mathrm{LDQ}}}{\mathrm{d}t} = v_{\mathrm{sDQ}} - Ri_{\mathrm{LDQ}} - j\omega_{\mathrm{s}}^{\mathrm{pu}}Li_{\mathrm{LDQ}} - V_2 \tag{15}$$

On the other hand, the model for the series-compensated transmission system is obtained from the application of KVL between V_{PCC} and V_2. In addition, the model of this transmission system must consider the series capacitor dynamics. The model is given by:

$$\frac{L}{\omega_{\mathrm{b}}}\frac{\mathrm{d}i_{\mathrm{LDQ}}}{\mathrm{d}t} = v_{\mathrm{sDQ}} - Ri_{\mathrm{LDQ}} - j\omega_{\mathrm{s}}^{\mathrm{pu}}Li_{\mathrm{LDQ}} - V_{\mathrm{cDQ}} - V_2 \tag{16}$$

$$\frac{C}{\omega_{\mathrm{b}}}\frac{\mathrm{d}V_{\mathrm{cDQ}}}{\mathrm{d}t} = i_{\mathrm{LDQ}} - j\omega_{\mathrm{s}}^{\mathrm{pu}}CV_{\mathrm{cDQ}} \tag{17}$$

where L represents the inductance of the transmission line, i_{LDQ} is the current through the line, and V_{cDQ} is the voltage across the series capacitor (all in per unit). R and C denote the resistance and capacitance of the line (both in per unit), respectively, and $\omega_{\mathrm{s}}^{\mathrm{pu}}$ is the per-unit angular frequency.

2.6. Control system model

In DFIG, a cascade control structure is used. High- and low-level control loops are employed in the RSC and GSC. Higher loops are slower than inner loops. Furthermore, a PLL in a synchronous reference frame is used for synchronization (Kunjumuhammed et al., 2019). The proportional-integral controller is commonly used for SSR and SSCI studies in all these control loops.

In this work, we consider both high-level and low-level control loops. For high-level loops, the RSC controls the active and reactive power injected by the DFIG stator (Yan et al., 2020). Specifically, the rotor current on the d-axis controls the active power, while the rotor current on the q-axis controls the reactive power. A similar structure is applied to the GSC, where the high-level loops control the voltage at the DC link using the current on the d-axis of the LC filter and control the voltage or reactive power with the current on the q-axis (Fan and Miao, 2021; Kunjumuhammed et al., 2019). The following subsections describe these control loops, beginning with the PLL.

2.6.1. Phase-locked loop

Fig. 4 shows the PLL control that synchronizes the system with the grid. The differential equation associated with the PLL control is given by:

$$\frac{\mathrm{d}\Delta\theta_{PLL}}{\mathrm{d}t} = \Delta\omega \tag{18}$$

where $\Delta\theta_{PLL}$ represents the output angle of the PLL, which enables synchronization with the grid, and $\Delta\omega$ denotes the detected frequency deviation as influenced by the voltage component v_{sq}. In addition, the equations associated with PI control are given by:

$$\frac{\mathrm{d}x_{\mathrm{PI,PLL}}}{\mathrm{d}t} = K_{i,\mathrm{PLL}}v_{\mathrm{sq}} \tag{19}$$

$$\Delta\theta_{\mathrm{PLL}} = x_{\mathrm{PI,PLL}} + K_{\mathrm{p,PLL}}v_{\mathrm{sq}} \tag{20}$$

where $x_{\mathrm{PI,PLL}}$ denotes the state variable of the PI controller. v_{sq} is the stator voltage in the q axis. $K_{i,\mathrm{PLL}}$ and $K_{\mathrm{p,PLL}}$ are the integral and proportional gain of the controller, respectively.

In this case, the control is oriented to the PCC voltage, which means $v_{\mathrm{sq}} = 0$. It is important to note that DQ and dq indicate whether the variables are non-oriented or oriented for control, respectively.

2.6.2. Rotor side converter

This converter is located between DFIG's rotor and the DC link. The RSC control scheme is shown in Fig. 5. The scheme has two levels of control. For the high-level control loops, the outer control loops regulate the active and reactive power through the rotor current on the d-axis and the q-axis, respectively. Specific considerations must be taken into account to control the active and reactive powers of the stator. For instance, when considering control orientation, $P_{\mathrm{s}} = v_{\mathrm{sd}}i_{\mathrm{sd}}$. Additionally, it is assumed that $R_{\mathrm{s}} \approx \frac{\mathrm{d}\psi_{\mathrm{sdq}}}{\mathrm{d}t} \approx 0$, leading to the following simplification:

$$P_{\mathrm{s}} = -v_{\mathrm{sd}}\frac{L_{\mathrm{m}}}{L_{\mathrm{s}}}i_{\mathrm{rd}} \tag{21}$$

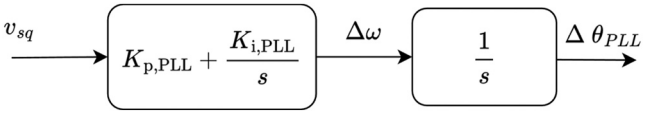


Fig. 4. PLL scheme control.

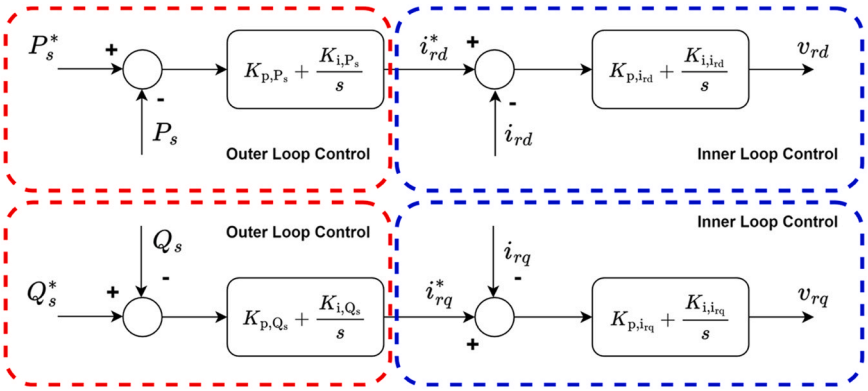


Fig. 5. RSC scheme control.

where v_{sd} represents the d-axis stator voltage, L_m is the mutual inductance of the windings, L_s is the stator inductance, and i_{rd} is d-axis rotor current (all in per unit). The equations representing the PI control of the active power injected by the stator are given by:

$$\frac{dx_{PI,\ P_s}}{dt} = K_{i,\ P_s}\left(P_s^* - P_s\right) \tag{22}$$

$$i_{rd}^* = x_{PI,\ P_s} + K_{p,\ P_s}\left(P_s^* - P_s\right) \tag{23}$$

where $x_{PI,\ P_s}$ represents the state variable of the PI controller. P_s^* and P_s are the reference and actual active power injected by the stator, respectively. i_{rd}^* is the reference rotor current on the d-axis (all in per unit). $K_{i,\ P_s}$ and $K_{p,\ P_s}$ are the integral constant and the proportional gain of the controller, respectively.

An important observation from this expression is that the rotor current in the direct axis must be negative if active power injection is desired. Similarly, the reactive power becomes $Q_s = -v_{sd}i_{sq}$. Expressing i_{sq} as a function of i_{rq} and v_{sd}, the reactive power is given by:

$$Q_s = \frac{L_m}{L_s}v_{sd}i_{rq} - \frac{v_{sd}^2}{L_s} \tag{24}$$

where i_{rq} is the q-axis rotor current (in per unit). Thus, if reactive power injection is desired, the rotor power in the q-axis must be increased. The parameters of the outer control loops are adjusted through a trial-and-error procedure, selecting values that enable appropriate dynamic performance.

The equations representing the PI control of the reactive power injected by the stator are given by

$$\frac{dx_{PI,\ Q_s}}{dt} = K_{i,\ Q_s}\left(Q_s^* - Q_s\right) \tag{25}$$

$$i_{rq}^* = x_{PI,\ Q_s} + K_{p,\ Q_s}\left(Q_s^* - Q_s\right) \tag{26}$$

where $x_{PI,\ Q_s}$ denotes the state variable of the PI controller. Q_s^* and Q_s are the reference and actual reactive power injected by the stator, respectively. i_{rq}^* is the reference rotor current on the q-axis (all in per unit). $K_{i,\ Q_s}$ and $K_{p,\ Q_s}$ are the integral and proportional gain of the controller.

The low-level loops commonly used are the current controllers. These generate the reference to the VSC. The dynamic response is fast, typically in the order of 20 ms or lower. In the RSC, the DFIG model is used. The current control loops neglect cross-coupling and feedforward terms. The output of the current control loops is the rotor voltage on its respective axis. Defining Defining $\sigma = 1 - \frac{L_m^2}{L_s L_r}$ and considering the same assumptions for the outer loop, the new equation for the controlled plant is given by:

$$u_{rd} = v_{rd} - \frac{L_m}{L_s}\omega_{SL}^{pu}v_{sd} - \omega_{SL}^{pu}\sigma L_r i_{rq} \tag{27}$$

where u_{rd} is the voltage in the VSC of the RSC in the reference voltage of the d axis (in per unit). It is important to mention that the procedure defines the plant on the q axis. v_{rd} is the voltage of the rotor on the d axis and L_r is the inductance of the rotor. Rewriting the DFIG rotor equation leads to the equation of the plant being controlled.

$$u_{rd} = -R_r i_{rd} - \sigma\frac{L_r}{\omega_b}\frac{di_{rd}}{dt} \tag{28}$$

The transfer function associated with the plant $H_{inner,RSC}$ is given by:

$$H_{inner,RSC} = \frac{-1/R_r}{s\frac{\sigma L_r}{R_r\omega_b} + 1} \tag{29}$$

The equations representing the PI control of the rotor current on the d-axis are given by:

$$\frac{dx_{PI,\ i_{rd}}}{dt} = K_{i,i_{rd}}\left(i_{rd}^* - i_{rd}\right) \tag{30}$$

$$v_{rd} = x_{PI,\ i_{rd}} + K_{p,i_{rd}}\left(i_{rd}^* - i_{rd}\right) \tag{31}$$

where $x_{PI,\ i_{rd}}$ represents the state variable of the PI controller. i_{rd}^* and i_{rd} are the reference and actual rotor currents, respectively, on the d-axis. v_{rd} is the rotor voltage on the d axis (all in per unit). $K_{i,i_{rd}}$ and $K_{p,i_{rd}}$ are the integral and proportional gain of the controller, respectively.

The equations representing the PI control of the rotor current on the q -axis are given by:

$$\frac{dx_{PI,\ i_{rq}}}{dt} = K_{i,i_{rq}}\left(i_{rq}^* - i_{rq}\right) \tag{32}$$

$$v_{rq} = x_{PI,\ i_{rq}} + K_{p,i_{rq}}\left(i_{rq}^* - i_{rq}\right) \tag{33}$$

where $x_{PI,\ i_{rq}}$ represents the state variable of the PI controller. i_{rq}^* and i_{rq} are the reference and actual rotor currents, respectively, on the q-axis. v_{rq} is the rotor voltage on the q axis (all in per unit). $K_{i,i_{rq}}$ and $K_{p,i_{rq}}$ are the integral and proportional gain of the controller, respectively.

2.6.3. Grid side converter

The GSC is located between the DC link and the LC filter. The control scheme of this converter is shown in Fig. 6, with two levels of control. In high-level control loops, an outer loop regulates the DC link voltage through the current of the filter on the d-axis. The other loop may regulate the reactive power of the GSC (setting a null reference) or the AC voltage of the PCC through the current of the filter on the q-axis, as shown in Fig. 7.

For the outer control loop of the GSC, the dynamics of the DC link

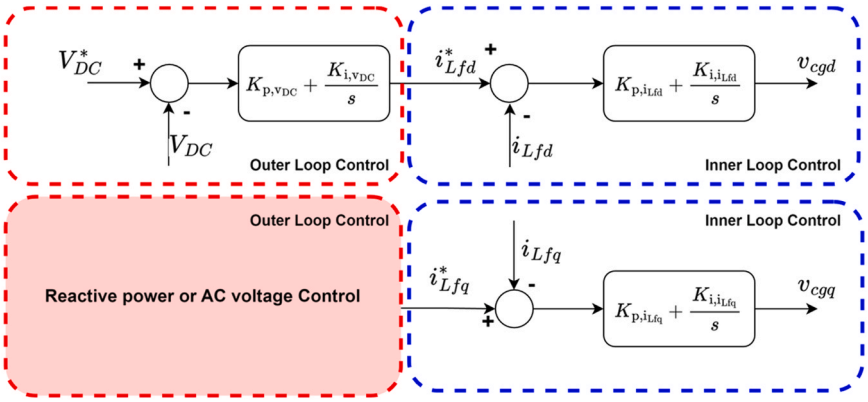


Fig. 6. GSC scheme control.

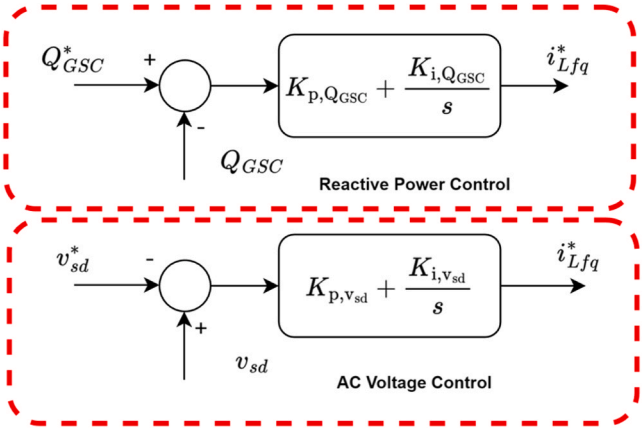


Fig. 7. Control schemes of the outer loop of the GSC.

must be considered. Since this equation is nonlinear, it must be linearized. Before that, P_{gsc} is rewritten as $v_{cgD} i_{LfD}$. The linearized expression is given by:

$$\frac{C_{DC}}{\omega_b}\frac{d\Delta v_{DC}}{dt} = -\Delta i_{Lfd} \tag{34}$$

where Δv_{DC} represents a small deviation in the DC link voltage (in per unit), while i_{Lfd} denotes a small deviation in the LC filter's d-axis current (in per unit). This expression defines the plant equation to be controlled. Applying the Laplace transform, the plant transfer function is:

$$H_{DC} = \frac{\Delta V_{DC}}{\Delta I_{LfD}} = -\frac{1}{\frac{C_{DC}}{\omega_b}s} \tag{35}$$

where H_{DC} is the transfer function of the DC link. The equations representing the PI control of DC link voltage are given by

$$\frac{dx_{PI,\ v_{DC}}}{dt} = K_{i,v_{DC}}\left(v^*_{DC} - v_{DC}\right) \tag{36}$$

$$i^*_{Lfd} = x_{PI,\ v_{DC}} + K_{p,v_{DC}}\left(v^*_{DC} - v_{DC}\right) \tag{37}$$

where $x_{PI,\ v_{DC}}$ represents the state variable of the PI controller. v^*_{DC} and v_{DC} are the reference and actual DC link voltages, respectively. i^*_{Lfd} is the reference current of the LC filter on the d-axis (all in per unit). $K_{i,v_{DC}}$ and $K_{p,v_{DC}}$ are the integral and proportional gain of the controller, respectively.

The equations representing the PI control of the GSC reactive power are given by:

$$\frac{dx_{PI,\ Q_{gsc}}}{dt} = K_{i,Q_{gsc}}\left(Q^*_{gsc} - Q_{gsc}\right) \tag{38}$$

$$i^*_{Lfq} = x_{PI,\ Q_{gsc}} + K_{p,Q_{gsc}}\left(Q^*_{gsc} - Q_{gsc}\right) \tag{39}$$

where $x_{PI,\ Q_{gsc}}$ represents the state variable of the PI controller. Q^*_{gsc} and Q_{gsc} are the reference and actual reactive powers of GSC, respectively. i^*_{Lfq} is the LC filter reference current on q-axis (all in per unit). $K_{p,Q_{gsc}}$ and $K_{i,Q_{gsc}}$ are the proportional and integral gain of the controller, respectively.

The equations representing the PI control of voltage at the PCC are given by:

$$\frac{dx_{PI,\ v_{sd}}}{dt} = K_{i,v_{sd}}\left(v^*_{sd} - v_{sd}\right) \tag{40}$$

$$i^*_{Lfq} = x_{PI,\ v_{sd}} + K_{p,v_{sd}}\left(v^*_{sd} - v_{sd}\right) \tag{41}$$

where $x_{PI,\ v_{sd}}$ represents the state variable of PI controller. v^*_{sd} and v_{sd} are the reference and actual PCC voltages, respectively, on the d-axis. i^*_{Lfq} is the reference current of the LC filter on the q axis (all in per unit). $K_{i,v_{sd}}$ and $K_{p,v_{sd}}$ are the integral and proportional gain of the controller, respectively. The low-level loops, which control the current, ignore cross-coupling and feedforward terms. The output of the current control loops is the voltage at the GSC's output on its respective axis. For the inner control loop, the equation of the LC filter is considered as follows:

$$u_d = v_{cgd} - v_{sd} + L_f \omega_e^{pu} i_{Lfq} \tag{42}$$

where u_d is the d-axis reference voltage (in per unit), v_{cgd} is the voltage at the GSC output (in per unit), and i_{Lfq} is the q-axis current through the LC filter (in per unit).

Considering this new term, the filter equation is rewritten as:

$$u_d = \frac{L_f}{\omega_b}\frac{di_{Lfd}}{dt} + R_f i_{Lfd} \tag{43}$$

where i_{Lfd} is the d-axis current through the LC filter (in per unit). With this expression, the transfer function is defined as:

$$H_{inner,GSC} = \frac{I_{Lfd}}{U_d} = \frac{1}{R_f + \frac{L_f}{\omega_b}s} \tag{44}$$

Here, $H_{inner,GSC}$ is the transfer function of the plant to be controlled. The equations representing the PI control of the LC filter current on the d-axis are given by:

$$\frac{dx_{PI,\ i_{Lfd}}}{dt} = K_{i,i_{Lfd}}\left(i^*_{Lfd} - i_{Lfd}\right) \tag{45}$$

$$v_{\mathrm{cgd}} = x_{\mathrm{PI},\ i_{\mathrm{Lfd}}} + K_{p,i_{\mathrm{Lfd}}}\left(i^{*}_{\mathrm{Lfd}} - i_{\mathrm{Lfd}}\right) \tag{46}$$

where $x_{\mathrm{PI},\ i_{\mathrm{Lfd}}}$ represents the state variable of PI controller on the d-axis. i^{*}_{Lfd} and i_{Lfd} are the reference and actual LC filter currents, respectively, on the d-axis. v_{cgd} represents the GSC output voltage on the d-axis (all in per unit). $K_{i,i_{\mathrm{Lfd}}}$ and $K_{p,i_{\mathrm{Lfd}}}$ are the integral and proportional gain of the controller, respectively.

The equations representing the PI control of the LC filter current on the q -axis are given by:

$$\frac{\mathrm{d}x_{\mathrm{PI},\ i_{\mathrm{Lfq}}}}{\mathrm{d}t} = K_{i,i_{\mathrm{Lfq}}}\left(i^{*}_{\mathrm{Lfq}} - i_{\mathrm{Lfq}}\right) \tag{47}$$

$$v_{\mathrm{cgq}} = x_{\mathrm{PI},\ i_{\mathrm{Lfq}}} + K_{p,i_{\mathrm{Lfq}}}\left(i^{*}_{\mathrm{Lfq}} - i_{\mathrm{Lfq}}\right) \tag{48}$$

where $x_{\mathrm{PI},\ i_{\mathrm{Lfq}}}$ represents the state variable of the PI controller on the q-axis. i^{*}_{Lfq} and i_{Lfq} are the reference and actual LC filter currents, respectively, on the q-axis. v_{cgq} represents the GSC output voltage on the q-axis (all in per unit). $K_{i,i_{\mathrm{Lfq}}}$ and $K_{p,i_{\mathrm{Lfq}}}$ are the integral and proportional gain of the controller, respectively.

3. Case studies and results

This section presents the case studies and the results obtained from modal analysis to study SSR in the test system depicted in Fig. 1. Modal analysis is an analytical method for assessing small signal stability and determining the root cause of SSR. This is done by analyzing the participation factors obtained from the modal analysis to allow for determining state variables. This technique is chosen because it is a well-known and acceptable method for SSR assessment (Vega-Herrera et al., 2021; Vega-herrera et al., 2024; Kunjumuhammed et al., 2016, 2017; Fan, 2019).

In order to perform modal analysis, the system must be linear. As the test system model is nonlinear, the test system needs to be linearized around a steady-state operating point. Numerical linearization is done in this study, as in (Vega-Herrera et al., 2021; Vega-herrera et al., 2024; Kunjumuhammed et al., 2016, 2017; Fan, 2019). The test system model described in 2 is implemented in MATLAB/Simulink and is linearized using the Linear Analysis Tool. Specifically, the "linearize" function is used to compute the state-space matrices numerically. Readers are referred to ($author1$ et al., 2019) for a detailed process description.

3.1. Description of case studies

This work considers four cases, as described in Table 1. Case 1 and Case 2 are conducted with SW1 closed and SW2 open simultaneously, meaning there is no series-compensated transmission line. In these cases, the impact of the PLL and the weakness of the system is studied. Accordingly, the line reactance varies from 0.01 to 0.7 pu, and the PLL bandwidth from 2 to 60 Hz.

Case 3. and Case 4 consider the series-compensated transmission line conducted simultaneously by SW2 closed and SW1 open (see Fig. 1). The integral constant K_{i} of the RSC and the compensation level are modified for these cases. The former takes values from −350 to −50, and the latter takes values from 5 % to 90 %. Compensation levels of 90 % are not common in real-life applications; however, the 90 % compensation level is included not as a typical real-world operating point but as an extreme case to define the stability region's boundary and assess each control strategy's resilience (Task Force on Wind SSO, 2020; Xie et al., 2017; Leon and Solsona, 2015).

The initial control parameters are shown in Table 3 in the Appendix. The PI controllers in the inner and outer control loops of DFIG described in 2 are determined by iterative tuning based on modal analysis. The gain values that provided satisfactory small-signal dynamic performance under nominal operating conditions ensuring well-damped dominant modes, are identified by trial and error. While this procedure does not constitute an analytical tuning method, it provides a consistent basis for comparing the dynamic behavior of the two outer-loop control strategies evaluated in this study. The proportional and integral constants related to the PI of the PLL are determined using the design tuning process shown in the Appendix. This process uses the PLL bandwidth and the damping coefficient as control criteria (Sun et al., 2019; Teodorescu et al., 2011; Blaajberg, 2018; Henríquez et al., 2025). It is considered for the cases where the impact of the PLL bandwidth is studied.

Switches SW1 and SW2 represent different network configurations of the test system, as shown in Fig. 1, and are not explicitly modeled. Instead, two nonlinear models are implemented in MATLAB/Simulink. The first model has SW1 closed and SW2 open, omitting the RLC branch (see Fig. 1). The second model has SW1 open and SW2 closed, omitting the RL branch (see Fig. 1).

Finally, it should be noted that the process follows for any change in control parameters. First, the power flow is calculated. Second, the steady-state operating point is determined. Finally, the system is linearized, as indicated at the beginning of 3. This process is kept for all the cases.

3.2. Results

This section compares two control schemes implemented in the outer control loop of the GSC. One scheme uses reactive power control, while the other uses PCC voltage control. The outputs of these control strategies are used to generate the q-axis reference filter current. DC link control is also performed for both control schemes, which provides the d-axis reference filter current.

3.2.1. Comparison between Case 1 and Case 2

In these cases, a sensitivity analysis of the transmission line reactance and the PLL bandwidth is performed, focusing on the M_A mode. The rest of the parameters take the values shown in Table 3. Fig. 8 illustrates the eigenvalue trajectories for each control strategy. In this figure, the circle "o" indicates the starting point of the mode trajectory, the cross "x" marks the trajectory, and the diamond "◆" signifies the end of the trajectory.

As shown in Fig. 8, the mode trajectories for both control strategies are similar. As the transmission line reactance and the PLL bandwidth increase, the mode shifts to the right, leading to small-signal instability at a PLL bandwidth of 60 Hz and a line reactance of 0.6 pu. However, differences in the mode characterization are observed between the two control strategies. For example, the oscillation frequency range for reactive power control is 20–50 Hz, whereas it is 22–46 Hz for voltage

Table 1
Case studies and sensitivity parameters.

Sensitivity parameters	Case 1: GSC Reactive Power Control (SW1 Closed)	Case 2: GSC PCC Voltage Control (SW1 Closed)	Case 3: GSC Reactive Power Control (SW2 Closed)	Case 4: GSC PCC Voltage Control (SW2 Closed)
Line reactance	0.01–0.7 pu	0.01–0.7 pu	-	-
PLL bandwidth	2–60 Hz	2–60 Hz		
K_{i} of the RSC inner loop	-	-	−50 to −350	−50 to −350
Level compensation	-	-	5–90 %	5–90 %

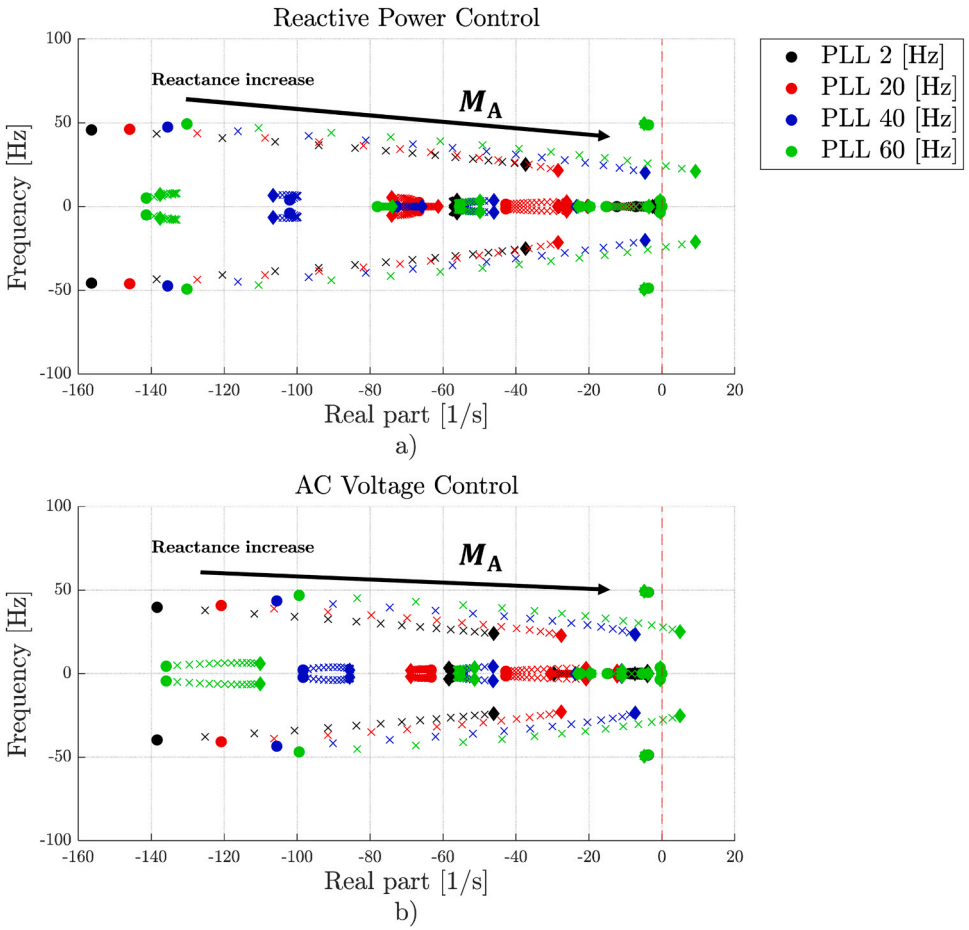


Fig. 8. Eigenvalue trajectories of the system with increasing transmission line reactance for different PLL bandwidths. (a) Reactive power control, (b) PCC voltage control.

control. There are also minor differences in mode damping between the two strategies. As line reactance increases, damping worsens for both strategies, with a critical deterioration at a PLL bandwidth of 40 Hz. The damping is 2.41 % for reactive power control at a reactance of 0.55 pu. The damping is 3.37 % for voltage control at a reactance of 0.5 pu. Although the differences are not substantial, reactive power control demonstrates slightly better mode damping in weak grids compared to PCC voltage control.

The participation factor analysis reveals similar results for both control strategies. The state variables involved in this mode include rotor flux, GSC and RSC current loops, and the transmission system. As the PLL bandwidth and line reactance increase, the participation of the transmission system, GSC, RSC, and PLL becomes more significant.

3.2.2. *Comparison between Case 3 and Case 4*

In these cases, a sensitivity analysis of two parameters is conducted. One is the integral constant of the internal current loop of the RSC. Another parameter is the compensation level of the transmission line. The rest of the parameters take the values shown in Table 3. The critical mode in these studies is the M_A mode, with the eigenvalue trajectories presented in Fig. 9.

In general, the mode trajectories are similar for both control strategies. In reactive power control, decreasing the magnitude of K_i and increasing the compensation level negatively affects the system. Instability occurs at certain K_i values and compensation levels. In particular, when K_i is -300 and compensation levels of 50 %, 60 %, and 65 %. When K_i is -200, the mode exhibits good damping for low compensation levels. Initially, the mode has a damping of 6.13 % and deteriorates to 1.28 % for 60 % compensation. The mode damping improves for compensation levels higher than 60 %, with oscillation frequencies ranging from 15 to 24 Hz. In contrast, when the PCC voltage control is considered, the system is small signal stable for the same cases as reactive power control. However, decreasing the integral constant K_i and increasing the compensation level reduces the damping coefficient lower. Thus, the dynamic performance of the system is worsened. Initially, the mode has a damping of 9.37 % for K_i of -200; when the compensation level reaches 60 %, the damping is 3.25 %. For compensation levels higher than this, damping improves, with oscillation frequencies ranging from 21 to 24 Hz.

The participation factor analysis between both control strategies is practically the same. For low compensation levels, there is interaction between the rotor flux, PLL, and GSC current loops and slightly with the transmission system. As the compensation level increases, the participation of the rotor flux decreases significantly, while participation from the transmission system, particularly the current and voltage of the capacitor, increases. Furthermore, as the magnitude of K_i increases, the rotor flux interaction decreases, and the current loop of the RSC gains more participation, leading to a high interaction between the GSC, PLL, RSC, and the transmission system.

For the comparison between Case 3 and Case 4, the results of both control strategies show significant differences. Reactive power control exhibits a reduced stability range. As the magnitude of K_i of the RSC increases, the system is more likely to be unstable. Specifically, the critical RSC values K_i where instability occurs are -250, -300, and -350. However, these instabilities occur for critical compensation levels between 40 % and 65 %. In contrast, PCC voltage control provides a wider stability range and has no instability for the cases studied.

The findings reported in (Leon and Solsona, 2015) indicate that

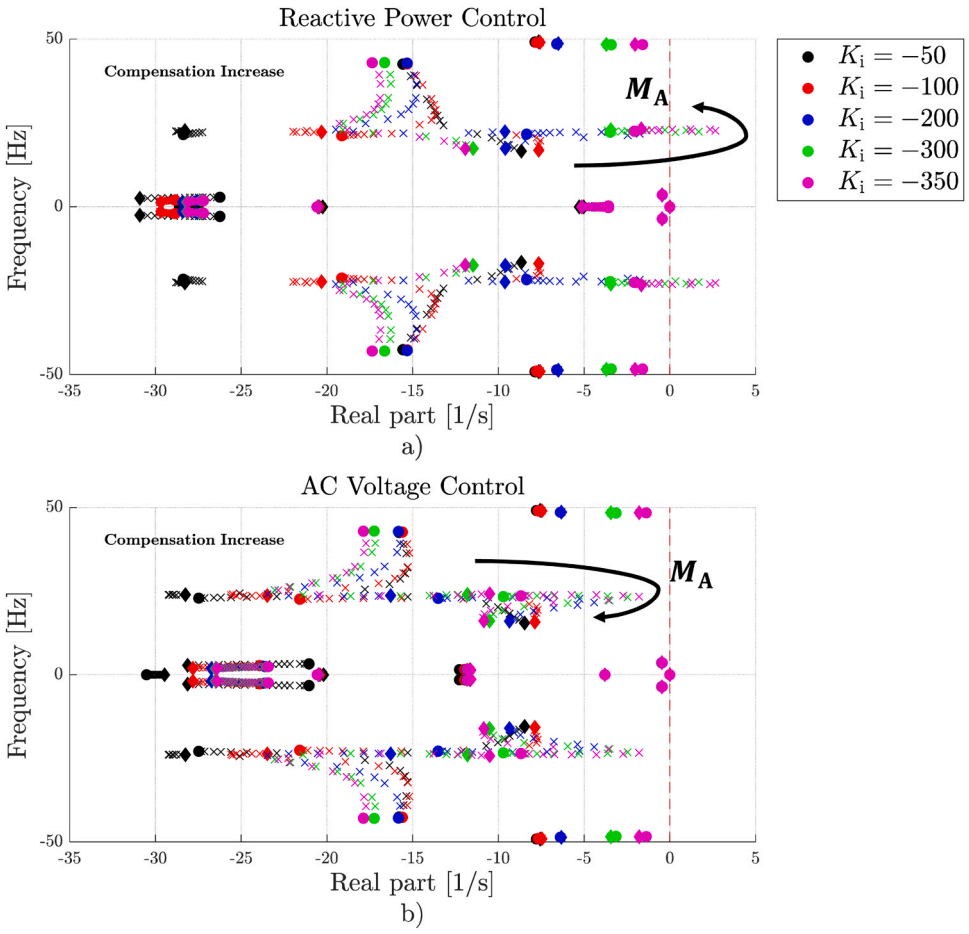


Fig. 9. Eigenvalue trajectories of the system with increasing compensation level for different Ki of the internal RSC loop. a) Reactive power control. b) PCC voltage control.

increasing the gain of the RSC control can cause system instability. This is consistent with the results presented in this work. However, reference (Leon and Solsona, 2015) also suggests that increasing the compensation level shifts the mode to the right, potentially causing instability at specific gain values. This phenomenon is not observed in this work. For voltage control, the mode shifts to the right (without becoming unstable), but as the compensation level increases, the mode shifts to the right up to 50 % compensation for the highest K_i value. For higher compensation levels, the mode shifts to the left. In the case of reactive power control, the trend is similar, but the mode becomes unstable (see Fig. 9).

The results obtained show that the DFIG control parameters can affect the stability of the system. However, the control strategy chosen for this type of power plant could impact the stability of the power system.

3.2.3. *Dynamic simulations*

In this section, the main results obtained from the modal analysis are validated by simulating the dynamic response of the test system. The complete nonlinear model is used. As mentioned in the previous section, significant differences arise when the DFIG is connected via a compensated transmission line. This corresponds to Case 3 and Case 4. For this reason and brevity, this section presents dynamic simulations for those cases. The small perturbation considered is a decrease of 0.1 % in the voltage magnitude V_2 (see Fig. 1). The parameter values selected to validate the results obtained by dynamic simulations are shown in Table 2. It includes four values for the integral constant K_i related to the RSC and compensation levels between 40 % and 65 %.

Fig. 10 shows the PCC voltage V_{PCC} simulated when reactive power control is used in the DFIG. It can be seen that as K_i decreases, the system becomes poorly damped, leading to system instability. This is accentuated as the level of compensation also increases. This observation aligns with the eigenvalue trajectories in Fig. 9(a) since the mode M_A is placed on the positive half-plane of the complex plane for these operating conditions. In contrast, Fig. 11 shows the PCC voltage V_{PCC} simulated when voltage control is considered in the DFIG. These simulations show that the system remains small-signal stable for all the K_i and compensation levels. This is expected because, for these operating conditions, the mode M_A is placed on the complex plane's negative half-plane, as shown in Fig. 9(b). Further, the oscillations are well damped. Overall, the simulations validate the observations made from modal analysis.

Table 2
Critical values in small-signal stability.

K_i of RSC	-200	-250	-300	-350
Compensation level	40–65 %			

4. Conclusions

This paper comprehensively compared reactive power and AC voltage control associated with the GSC of the DFIG connected to a weak system and series-compensated transmission lines. The modal analysis results reveal that the AC voltage control consistently outperforms the reactive power control by providing enhanced damping characteristics and maintaining stability in various compensation levels and current controller parameters. In particular, AC voltage control demonstrated

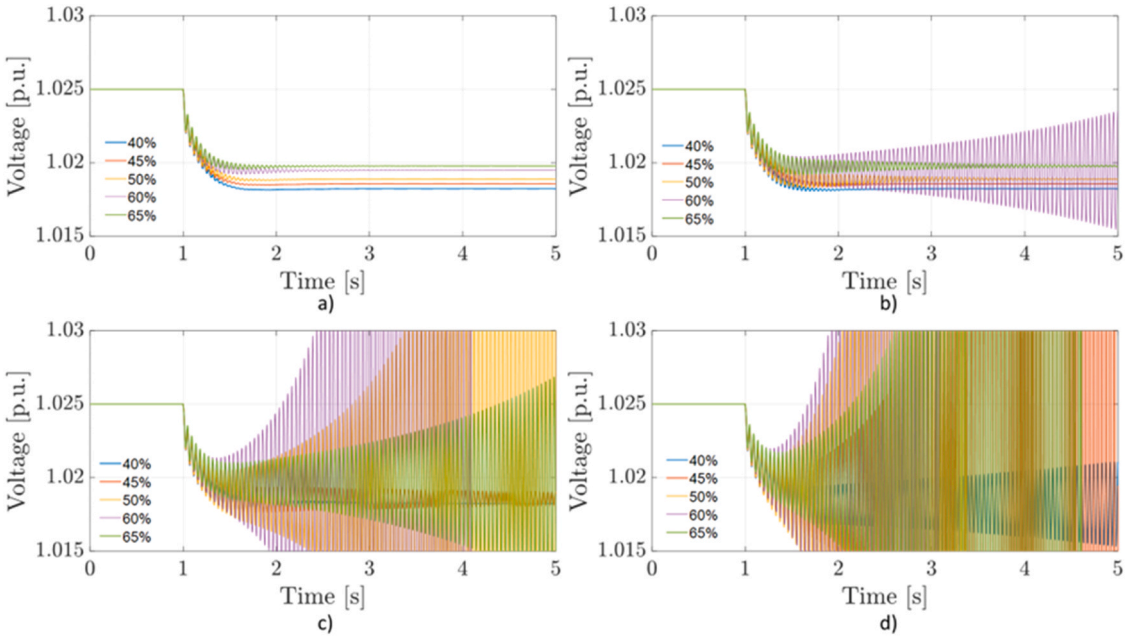


Fig. 10. Dynamic simulations of the PCC voltage for different compensation levels, considering reactive power control. (a) K_i of −200, (b) K_i of −250, (c) K_i of −300, (d) K_i of −350.

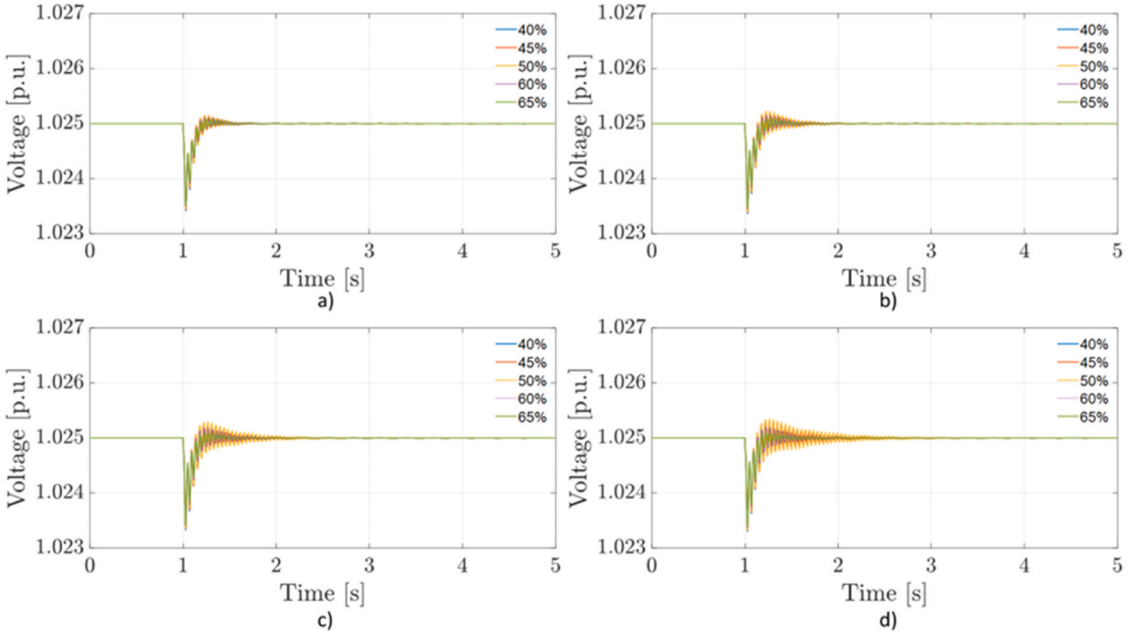


Fig. 11. Dynamic simulations of the PCC voltage for different compensation levels, considering PCC voltage control. (a) K_i of −200, (b) K_i of −250, (c) K_i of −300, (d) K_i of −350.

superior performance in mitigating SSR issues, allowing higher compensation levels than reactive power control. In the case of weak conditions without series compensations, both control strategies have no significant differences, making the PLL's bandwidth more relevant. Dynamic simulations validate and verify the main observations from modal analysis. This paper provides valuable insights for enhancing the design and control of DFIG-based wind farms, contributing to the broader effort to ensure the dependable operation of renewable energy systems in modern power grids. Future research will explore integrating adaptive control techniques and the application of Hardware in the Loop methods for validation.

Authorship contributions

Category 1

Conception and design of study: *J. Vega-Herrera, S. Fuentes-Flores;* acquisition of data: *J. Vega-Herrera, S. Fuentes-Flores*; analysis and/or interpretation of data: *J. Vega-Herrera, S. Fuentes-Flores;*

Category 2

Drafting the manuscript: *J. Vega-Herrera, S. Fuentes-Flores, A. Villamarín-Jacóme;* revising the manuscript critically for important

intellectual content: *D. Ortiz-Villalba, J. Llanos, M. Cortes Carmona, D. Espín-Sarzosa.*

Category 3

Approval of the version of the manuscript to be published: *J. Vega-Herrera, S. Fuentes-Flores, D. Ortiz-Villalba, J. Llanos, A. Villamarín-Jacóme, M. Cortes Carmona, and D. Espín-Sarzosa.*

Authorship statement

All persons who meet authorship criteria are listed as authors, and all authors certify that they have participated sufficiently in the work to take public responsibility for the content, including participation in the concept, design, analysis, writing, or revision of the manuscript. Furthermore, each author certifies that this material or similar material has not been and will not be submitted to or published in any other publication before its appearance in the *journal Energy Reports*.

CRediT authorship contribution statement

Ortiz-Villalba Diego: Writing – review & editing, Supervision, Methodology, Funding acquisition, Conceptualization. **Vega-Herrera Jorge:** Writing – original draft, Validation, Methodology, Investigation, Formal analysis, Conceptualization. **Villamarín-Jácome Alex:** Writing – review & editing, Supervision, Methodology. **Llano Jacquelines:** Writing – review & editing, Validation, Supervision, Methodology, Conceptualization. **Fuentes-Flores Stevens:** Investigation, Formal analysis, Conceptualization.

Declaration of Competing Interest

The authors declare that they have no known competing financial interests or personal relationships that could have appeared to influence the work reported in this paper.

Acknowledgements

The authors gratefully acknowledge the financial support from SERC Chile FONDAP/CONICYT grant number 1523A0006. Universidad de las Fuerzas Armadas ESPE" through the project Renewable generation system for island communities: sustainable clean energy considering cultural, ecological, economic, and resilience aspects.(2024-PIM-02)

Appendix A. Initial control parameters

The initial control parameters used for the initial work for modeling DFIG are shown in Table 3. If it is not indicated, all the parameters are in pu expressed on a proper base.

Table 3
Definition of system parameters

Parameter	
Base power: S_b	100 MVA
Base line voltage: V_{Lb}	16.5 kV
System frequency: f_b	50 Hz
Base electrical speed: ω_b	$2\pi f_b$
Mechanical transmission system	
Inertia constant of generator and turbine: H_g and H_t.	0.9 s, 4.29 s
Damping coefficient of the drive train, turbine and generator; D_{tg}, D_t and D_g.	1.5, 0, 0
Stiffness of the drive system: k_{tg}.	751
Doubly Fed Induction Generator	
Stator and rotor resistance: R_s and R_r	0.00488
	0.00549
Stator and rotor leakage inductance: X_{ls} y X_{lr}.	0.09231
	0.09955
Mutual inductance of windings: X_m.	3.95279
Stator and rotor inductance: X_s and X_r.	4.0451
	4.05234
LC filter	
Filter series and damping resistance: R_f and R_d.	0.016
	0.1
Filter inductance: L_f.	0.2
Filter capacitor: C_f	0.1
RSC control parameters	
Proportional and integral inner loop constant: $K_{p,\ i_{rd}}$ ($K_{p,\ i_{rq}}$) and $K_{i,\ i_{rd}}$ ($K_{i,\ i_{rd}}$)	−1
	−50
Proportional and integral outer active power control loop constants: $K_{p,\ P_s}$ and $K_{i,\ P_s}$	0
	−22
Proportional and integral outer reactive power control loop constants: $K_{p,\ Q_s}$ and $K_{i,\ Q_s}$	0
	22
DC link	
Capacitor del DC link: C_{DC}	2
GSC control parameters	
Proportional and integral inner loop constant: $K_{p,\ i_{Lfd}}$ ($K_{p,\ i_{Lfq}}$) and $K_{i,\ i_{Lfd}}$ ($K_{i,\ i_{Lfq}}$)	0.5306
	239.4622
Proportional and integral outer loop constants for reactive power control: $K_{p,\ v_{DC}}$ and $K_{i,\ v_{DC}}$	−0.060848
	−0.18719
Proportional and integral outer loop constants for reactive power control: $K_{p,\ Q_{gsc}}$ and $K_{i,\ Q_{gsc}}$	−1.1614
	−172

(*continued on next page*)

Table 3 (*continued*)

Parameter	
Proportional and integral outer loop constants for AC voltage control: $K_{p,\ v_{sd}}$ and $K_{i,\ v_{sd}}$	0.25 25
PLL control parameters	
Proportional and integral constants: $K_{p,PLL}$ and $K_{i,PLL}$	10 30

Appendix B. PLL design

The design is based on time-domain criteria, considering the damping factor ξ and bandwidth frequency f_{-3dB} as design criteria. The damping factor ξ is set to be equal to 0.707. In the study, typical PLL bandwidths f_{-3dB} between 2 Hz and 60 Hz are considered (Sun et al., 2019; Teodorescu et al., 2011; Blaajberg, 2018; Henríquez et al., 2025). For a specific PLL bandwidth $\omega_{-3dB} = 2\pi f_{-3db}$and damping factor, the value of ω_n is determined using (49). The values of ω_n and ξ enable the determination of $K_{p,PLL}$ and $K_{i,PLL}$ according to (50) and (51), respectively.

$$\omega_n = \left(1 + 2\xi^2 + \sqrt{\left(1 + 2\xi^2\right)^2 + 1}\right)^{-\frac{1}{2}} \omega_{-3dB} \tag{49}$$

$$K_{p,PLL} = 2\xi\omega_n \tag{50}$$

$$K_{i,PLL} = \omega_n^2 \tag{51}$$

Using (49)-(51), the proportional and integral gains of the PI controller associated with the PLL are obtained. Table 4 shows these constants.

Table 4
Proportional and integral gains of the PI controller of the PLL

Bandwidth frequency f_{-3dB} [Hz]	Proportional gain $K_{p,PLL}$	Integral gain $K_{i,PLL}$
2	36.57	668.84
20	365.69	66884.27
40	731.38	267537.08
60	1097.07	601958.43

Data availability

Data will be made available on request.

References

Abdeen, M., Li, H., Jing, L., 2020. Improved subsynchronous oscillation detection method in a DFIG-based wind farm interfaced with a series-compensated network. Int. J. Electr. Power Energy Syst. 119, 1–10. https://doi.org/10.1016/j.ijepes.2020.105930.

Blaajberg, F., 2018. "Chapter 2 - Basic control principles in power electronics: Analog and digital control design,". In: in Control of power electronic converters and systems, 1. Academic Press, pp. 31–68.

Cheng, Y., et al., 2022. Real-world subsynchronous oscillation events in power grids with high penetrations of inverter-based resources. IEEE Trans. Power Syst. 1–15. https://doi.org/10.1109/tpwrs.2022.3161418.

Cheng, Y., et al., 2023. Real-world subsynchronous oscillation events in power grids with high penetrations of inverter-based resources. IEEE Trans. Power Syst. 38 (1), 316–330. https://doi.org/10.1109/TPWRS.2022.3161418.

Din, Z., et al., 2022. Recent development and future trends of resonance in doubly fed induction generator system under weak grid. IET Renew. Power Gener. 16 (5), 807–834. https://doi.org/10.1049/rpg2.12378.

Fan, L., 2019. Modeling type-4 wind in weak grids. IEEE Trans. Sustain. Energy 10 (2), 853–863. https://doi.org/10.1109/TSTE.2018.2849849.

Fan, L., et al., 2022. Real-world 20-Hz IBR subsynchronous oscillations: signatures and mechanism analysis. IEEE Trans. Energy Convers. 37 (4), 2863–2873. https://doi.org/10.1109/TEC.2022.3206795.

Fan, L., Miao, Z., 2021. Analytical model building for Type-3 wind farm subsynchronous oscillation analysis. Electr. Power Syst. Res. 201, 1–12. https://doi.org/10.1016/j.epsr.2021.107566.

Fan, L., Zhu, C., Miao, Z., Hu, M., 2011. "Modal analysis of a DFIG-based wind farm interfaced with a series compensated network," (Dec.). IEEE Trans. Energy Convers. 26 (4), 1010–1020. https://doi.org/10.1109/TEC.2011.2160995.

Gu, K., Wu, F., Zhang, X.-P., 2019. Sub-synchronous interactions in power systems with wind turbines: a review. Inst. Eng. Technol. https://doi.org/10.1049/iet-rpg.2018.5199.

GWEC, "Global wind report 2024," 2024. [Online]. Available: ⟨www.gwec.net⟩.

Henríquez, R., Rahmann, C., Vega-Herrera, J., Vittal, V., Vega, B., 2025. A novel adaptive controller for one-stage PV power plants considering PLL dynamic performance. Energy Rep. 13, 670–679. https://doi.org/10.1016/j.egyr.2024.12.017.

Hussain, H.A., Loncarski, J., Ristic, L.B., Bellini, A., 2024. DFIG-based WECS with partial-scale converter: Efficiency, cost, and volume comparison of SiC-based and IGBT-based converter Solution. IEEE Access 12, 89908–89920. https://doi.org/10.1109/ACCESS.2024.3419810.

Irwin, G., Jindal, A., Isaacs, A., 2011. Sub-synchronous control interactions between type 3 wind turbines and series compensated AC transmission systems. 2011 IEEE Power Energy Soc. Gen. Meet. 1–6. https://doi.org/10.1109/PES.2011.6039426.

P.C. Krause, Oleg. Wasynczuk, S.D. Sudhoff, and Steven. Pekarek, Analysis of electric machinery and drive systems, 3rd ed. John Wiley & Sons, 2013.

Kunjumuhammed, L., Kuenzel, S., Pal, B., 2019. Wind turbine generator modelling. in Simulation of Power System with Renewables. Academic Press, pp. 133–180. https://doi.org/10.1016/b978-0-12-811187-1.00006-8 (ch. six).

Kunjumuhammed, L.P., Pal, B.C., Oates, C., Dyke, K.J., 2016. Electrical oscillations in wind farm systems: analysis and insight based on detailed modeling. IEEE Trans. Sustain. Energy 7 (1), 51–62. https://doi.org/10.1109/TSTE.2015.2472476.

Kunjumuhammed, L.P., Pal, B.C., Gupta, R., Dyke, K.J., 2017. Stability analysis of a PMSG-based large offshore wind farm connected to a VSC-HVDC. IEEE Trans. Energy Convers. 32 (3), 1166–1176. https://doi.org/10.1109/TEC.2017.2705801.

Leon, A.E., Solsona, J.A., 2015. Sub-synchronous interaction damping control for DFIG wind turbines (Jan.). IEEE Trans. Power Syst. 30 (1), 419–428. https://doi.org/10.1109/TPWRS.2014.2327197 (Jan.).

Liu, R., Yao, J., Pei, J., Wang, X., Sun, P., Guo, X., 2018. Dynamic stability analysis of the weak grid-connected DFIG-based wind turbines under severe symmetrical faults. in 2018 International Conference on Power System Technology, POWERCON 2018 - Proceedings. IEEE, Guangzhou, China, pp. 1512–1517. https://doi.org/10.1109/POWERCON.2018.8601827.

Loncarski, J., Hussain, H.A., Bellini, A., 2023. Efficiency, cost, and volume comparison of SiC-based and IGBT-based full-scale converter in PMSG wind turbine. Electronics 12 (2), 1–14. https://doi.org/10.3390/electronics12020385.

Okedu, K.E., 2022. Augmentation of DFIG and PMSG wind turbines transient performance using different fault current limiters. Energies 15 (13). https://doi.org/10.3390/en15134817.

Soomro, M., et al., 2023. Performance improvement of grid-integrated doubly fed induction generator under asymmetrical and symmetrical faults. Energies 16 (8), 1–20. https://doi.org/10.3390/en16083350.

Sun, Y., et al., 2019. The impact of PLL dynamics on the low inertia power grid: A case study of Bonaire island power system. Energies 12 (7), 1–16. https://doi.org/10.3390/en12071259.

Task Force on Wind SSO, "Wind energy systems sub- synchronous oscillations: Events and modeling," 2020. doi: 10.17023/faak-ta85.

R. Teodorescu, M. Liserre, and P. Rodriguez, Grid converters for photovoltaic and wind power systems. Hoboken, NJ, USA: John Wiley & Sons, 2011. doi: 10.1002/9780470667057.

Vega-herrera, J., et al., 2024. Impact of modeling photovoltaic power plants operating in grid forming mode on small-signal stability of power Systems. in 2024 IEEE Sixth Ecuador Technical Chapters Meeting (ETCM), pp. 1–6.

Vega-Herrera, J., Rahmann, C., Valencia, F., Strunz, K., 2021. Analysis and application of quasi-static and dynamic phasor calculus for stability assessment of integrated power electric and electronic systems. IEEE Trans. Power Syst. 36 (3), 1750–1760. https://doi.org/10.1109/TPWRS.2020.3030225.

Virulkar, V.B., Gotmare, G.V., 2016. Sub-synchronous resonance in series compensated wind farm: a review. Renew. Sustain. Energy Rev. 55, 1010–1029. https://doi.org/10.1016/j.rser.2015.11.012.

Wang, L., Xie, X., Jiang, Q., Liu, H., Li, Y., Liu, H., 2015. Investigation of SSR in practical DFIG-Based wind farms connected to a series-compensated power system. IEEE Trans. Power Syst. 30 (5), 2772–2779. https://doi.org/10.1109/TPWRS.2014.2365197.

Xie, X., Zhang, X., Liu, H., Liu, H., Li, Y., Zhang, C., 2017. Characteristic analysis of subsynchronous resonance in practical wind farms connected to series-compensated transmissions. IEEE Trans. Energy Convers. 32 (3), 1117–1126. https://doi.org/10.1109/TEC.2017.2676024.

Xu, Y., Zhao, S., 2019. Mitigation of subsynchronous resonance in series-compensated dfig wind farm using active disturbance rejection control. IEEE Access 7, 68812–68822. https://doi.org/10.1109/ACCESS.2019.2919561.

Yan, C., Yao, W., Wen, J., Fang, J., Ai, X., Wen, J., 2020. Modelling and comparison analysis of grid-connected DFIG-based wind farm in weak grid (Oct.). IET Renew. Power Gener. 14 (13), 2406–2415. https://doi.org/10.1049/iet-rpg.2019.1382 (Oct.).